PHYSICAL REVIEW E **110**, 044303 (2024)

Editors' Suggestion   Featured in Physics

Emergence of social phases in human movement

Yi Zhang,[1] Debasish Sarker,[1] Samantha Mitsven,[2] Lynn Perry,[2] Daniel Messinger,[2] Udo Rudolph,[3] Michael Siller,[4,5,*] and Chaoming Song[1,†]

[1]*Department of Physics, University of Miami, Coral Gables, Florida 33146, USA*
[2]*Department of Psychology, University of Miami, Coral Gables, Florida 33146, USA*
[3]*Department of Psychology, Chemnitz University of Technology, 09107 Chemnitz, Germany*
[4]*Department of Pediatrics, Emory University, Atlanta, Georgia 30322, USA*
[5]*Marcus Autism Center, Children's Healthcare of Atlanta, Atlanta, Georgia 30329, USA*

(Received 13 April 2024; accepted 16 August 2024; published 3 October 2024)

Recent empirical studies have found different thermodynamic phases for collective motion in animals. However, such a thermodynamic description of human movement remains unclear. Existing studies of traffic and pedestrian flows have primarily focused on relatively high-speed mobility data, revealing only a fluidlike phase. This focus is partly because the parameter space of low-speed movement, which is governed predominantly by pairwise social interaction, remains largely uncharted. Here, we used ultrawideband radio frequency identification (UWB-RFID) technology to collect high-resolution spatiotemporal data on movements in four different classroom and playground settings. We observed two unique social phases in children's movements: a gaslike phase of free movement and a liquid-vapor coexistence phase characterized by the formation of small social groups. We also developed a simple statistical physics model that can reproduce different empirically observed phases. The proposed UWB-RFID technology can also be used to study the dynamics of active matter systems, including animal behavior, coordinating robotic swarms, and monitoring human interactions within complex systems, potentially benefiting future research in social physics.

DOI: 10.1103/PhysRevE.110.044303

I. INTRODUCTION

Understanding collective movement dynamics represents a crucial focus within social physics, given its implications across fields in the biological sciences [1–8], social sciences [9–12], and epidemiology [13]. A myriad of studies in recent years have examined human crowds at varying scales. These studies span microscopic scales, including pedestrian flows examined via video [14,15], head tracking devices [16], Bluetooth scanning [17], and depth sensors [18–21] to macroscopic scales using methodologies such as banknote circulation [22], mobile-phone records [23–25], and GPS tracking [26,27].

Recent years have witnessed a substantial growth in quantitative analyses of pedestrian flows [28–30]. Existing studies primarily leverage crowds of voluntary participants asked to perform specific tasks and derive results from laboratory recordings. Seminal research suggests that mobile crowd flows exhibit fluidlike behavior [9,11,12,31–33], with velocities roughly aligning to the Maxwell-Boltzmann distribution. Indeed, pedestrian flow is mainly driven by relatively weak physical interactions among nearby individuals [34]. However, more recent research suggests that human crowds display more nuanced social behavior than existing studies where the crowd's primary focus is on movement [18,19,34–46]. In social contexts such as parties, conferences, and reunions, individuals may exhibit limited movement and social interaction may affect physical parameters in a detectable fashion [47,48]. From a physics perspective, these two contrasting scenarios may correspond to different phases with distinct intrinsic properties.

We explore the possibility that social interaction affects the physics of movement, a concept originally suggested through numerical simulation of the social force model, which proposes that human movement may undergo a liquid-vapor phase transition driven by social interaction [49–53]. Several animal studies support this hypothesis [3–5]. A recent study on coordinated movement in robotic swarms also suggest that interaction rules can significantly influence movement dynamics [54]. Nonetheless, the phase of human groups exhibiting low-speed movement, whose behavior may reflect social interactions, remains experimentally underexplored. Figure 1 summarizes the state-of-the-art phase diagram detailing average speed (v) and crowd density (ρ). As the figure shows, most current experiments primarily focus on the high-speed regime (speed >1 m/s). Unexplored is the possibility that a different phase could potentially emerge within low-speed regimes that may be affected by strong social interactions.

Here, we investigate the states characteristic of low-speed movement by conducting experiments with preschool children across four different data sets classified into three groups: low free-play classrooms, high free-play classrooms, and very high free-play playgrounds (colored symbols in Fig. 1). In

*Present address: College of Education, University of North Texas, Denton, TX 76201, USA.
†Contact author: c.song@miami.edu

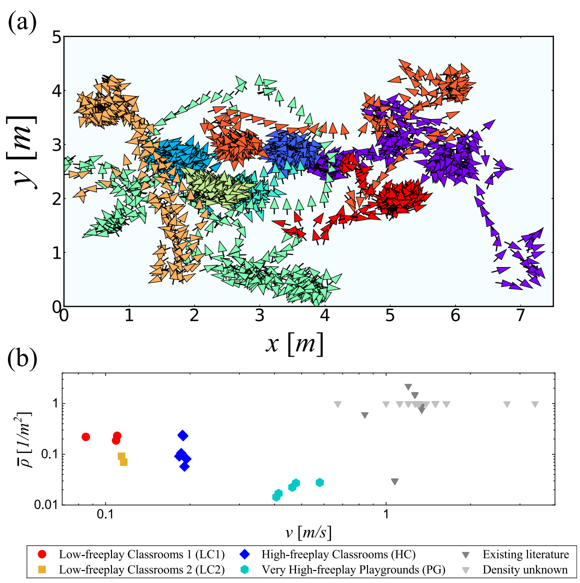

FIG. 1. Trajectories and speed-density diagram. (a) An illustration of 300 seconds of the trajectories of nine individuals from LC1. Colors and arrows identify the specific individuals and their orientations, respectively. (b) Colored scatter represents LC1 (red circle), LC2 (yellow square), HC (blue diamond), and PG (cyan hexagon), respectively. Gray triangles represent data measured in the existing literature [18,19,31,34–45]. The light gray triangles indicate studies with unrecorded densities of individual participants; these are set to $\rho = 1$ for the plot. Descriptions of the low free-play and high free-play classrooms, and very high free-play playgrounds, are contained in the text.

low free-play classrooms, children's movement is suppressed, and social communication dynamics may be more evident. In high free-play classrooms, movement is less constrained. Finally, in very high free-play playgrounds, children move relatively freely, aligning more closely with the pedestrian flow dynamics. Individuals in non-free-play activities are more directed and supervised than in free-play activities. Importantly, all groups exhibit omnidirectional motion, distinguishing this research from most existing studies. These experiments reveal differing behaviors in the three groups, quantified via measures such as radial distribution function (RDF) and local density distributions (LDDs). Our observations identify two distinct social phases at different speeds: (i) a gaslike phase where individuals move freely without forming small social groups and (ii) a liquid-vapor coexistencelike phase where individuals form small social groups, with free-moving individuals entering and exiting these groups [see Fig. 1(a)]. We find that the average speed in the gaslike social phase is significantly higher than that in the liquid-vapor coexistencelike phase. Lastly, we propose a social force model inspired by empirical data. Our model's numerical simulations successfully reproduce the empirically observed social phases. We further demonstrate that physical quantities measured in our model align qualitatively with experimental observations.

II. DATA COLLECTION

We collected human movement data sets in three schools (see Supplemental Material (SM) [55], Sec. A.2, Table S.1). Receivers in the corners of each classroom received ultrawideband radio frequency identification (UWB-RFID) signals at $2 \sim 4$ Hz, allowing continuous measurement of individual locations [56–58].

Low free-play classrooms 1 (LC1) comprises three academic years (2016-17, 2017-18, and 2018-19) of classroom movements in U.S. preschool A, involving 31 children aged 2.5 to 4 years. It includes 36 observations, each spanning two to four hours and tracking both spatial location (via vest tags) and orientation. Tracking of orientation was made possible by means of a dual tag setup, one on each side of vests worn by the children. Free-play activities occurred during 18% of the total observation time.

Low free-play classrooms 2 (LC2) is comparable to LC1, focusing on U.S. preschool B over two academic years (2018-19 and 2019-20). It includes 27 children and 25 independent observations. Free-play activities occurred during 20% of the total observation time.

High free-play classrooms (HCs) differ slightly from LCs, focusing on U.S. preschool C during the academic years 2021-22 and 2022-23. It involves a total of 80 children divided into three different age groups: 2, 3, and 4 years old. It comprises a total of 50 independent observations, each spanning two to four hours. In HCs, individuals were equipped with a single UBW-RFID tag allowing tracking of spatial movements only. Free-play activities in these classrooms ranged from 39% to 45% of the total observation duration.

The very high free-play playground (PG) documents unrestricted activities in the playground, featuring 71 children from HCs (excluding the three-year-olds from 2022-23), across three different age groups in 42 independent observations. These playground sessions were comparatively shorter, each lasting approximately 45 minutes. Similar to HCs, no orientation data was recorded in PGs, as both used a single-tag setup. Individuals in PG settings are free to move across a more expansive area, while those in classroom environments are involved in a lower proportion of free-play activities. Free-play activities in these PG settings are 100% of the total observation duration.

Missing data occurred at two levels. First, absences on observation days, which were minimal, were addressed by excluding all tracking information for absent children. Second, during data recording, short-term (< 60 s) data gaps caused by children removing their RFID tags, leaving the classroom, or signal loss were addressed using the Kalman filter algorithm to interpolate the data [59,60]. This ensured the data sets remained robust and continuous, maintaining the quality of our analysis and results.

A preliminary visualization [Fig. 1(a)] of nine individuals from LC1 during a continuous class time period shows that the participants are not uniformly located in the classroom space, suggesting they may form small social groups. The emergence of such groups is consistent over different observations with individuals joining and leaving the groups. It appears that the density of children varies both by physical location and over time. Furthermore, individuals' orientations, represented by their arrows, appear correlated within groups.

In our initial analysis, we measure the average speeds and densities across all data sets and juxtapose these findings with experiments previously reported in the literature, as

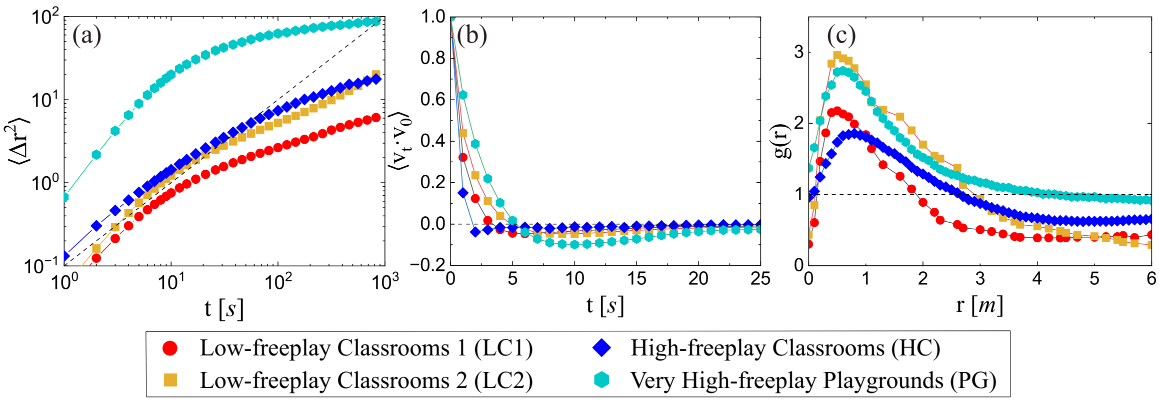

FIG. 2. Dynamic measures. (a) Mean square displacement $\langle\Delta r^2\rangle$, (b) velocity autocorrelation function $C_v(t)$, where dots represent experimental measures (see SM [55], Sec. B.1 for more details), and (c) radial distribution function $g(r)$ for all data sets.

illustrated in Fig. 1(b). Remarkably, our data sets predominantly occupy an unexplored domain characterized by low speeds ($v < 0.5$ m/s). This unique feature sets our study apart from earlier research. Within this low-speed regime, as depicted in Fig. 1(b), our data sets cluster into three distinct groups: LC1 and LC2, HC, and PG, each corresponding to different levels of free-play activity (see SM [55], Table S.1). The variations in free-play activity across these data sets correspond with different average speeds that may impact their dynamical and structural characteristics. For instance, dynamics within low free-play classrooms (LC1 and LC2) may be marked by higher levels of engagement and interaction. In the sections that follow, we examine a series of quantitative measures to further explore and characterize these trends.

All protocols were approved by the University of Miami IRB and Emory University IRB. Informed consent for participating students was obtained from their parents or legal guardians. Participant confidentiality and data anonymity were maintained throughout the study.

III. RESULTS

A. Dynamical measures

1. Mean square displacement

To explore the dynamics of individual movement, we first measure the mean square displacement (MSD), $\langle\Delta r^2\rangle$, that quantifies the diffusion in individual movement over time t. In the context of two-dimensional Brownian motion, the MSD adheres to a linear relationship, $\langle\Delta r^2\rangle \sim t$ [61]. Figure 2(a) presents the averaged MSD across all data sets. Our analysis reveals that the MSD values are markedly different between classroom (LC1, LC2, and HC) and PG data sets.

In classroom contexts, Fig. 2(a) illustrates distinct MSD scaling behaviors at various timescales. Specifically, at timescales on the order of seconds, all data sets reveal either superlinear or linear diffusion, with individuals exhibiting behavior akin to random walkers. Among them, the HC data set manifests the most rapid rate of diffusion. As we move to longer timescales, timescales that are orders of magnitude greater than 10 s, a transition to a sublinear diffusion regime occurs, characterized by $\langle\Delta r^2\rangle \sim t^\alpha$. Here, the exponent α, which ranges from approximately 0.3 to 0.6 (see SM [55], Sec. B.1), indicates a deceleration in motion. For extended durations, however, the pace of individual movement diminishes, a phenomenon likely induced by social interactions. Moreover, the displacements $\Delta r(t_s)$ at interaction times, measuring approximately 1.5m for LC1 and LC2 and 3m for HC, serve as rough estimates of the spatial dimensions of social groups.

In PG data sets, we observe markedly different MSD patterns compared to classroom settings, with $\langle\Delta r^2\rangle$ values that are an order of magnitude higher (see SM [55], Sec. B.2 for related statistical tests). On short timescales, the MSD exhibits a quadratic relationship approximately, $\langle\Delta r^2\rangle \propto t^2$, indicative of ballistic motion rather than diffusive behavior. This quadratic trend primarily stems from consistent, unidirectional movement at a constant speed as opposed to the random-walk diffusion typically observed in classrooms. Interestingly, a crossover phenomenon occurs at longer timescales, where the MSD in playgrounds reaches a saturation point at a physical boundary of about $(10\,\mathrm{m})^2$. This is in contrast to the classrooms, where diffusion has been slowed at a spatial scale of 2–3 meters before reaching the physical boundary. These observations highlight the differences between classroom and playground dynamics.

2. Velocity autocorrelation function

Concurrently, we measure the velocity autocorrelation function (VACF), $C_v(t) = \langle v(t)\cdot v(0)\rangle$, to quantify the temporal correlation in velocity over a time interval t. For Brownian particles, the VACF typically exhibits an exponential decay pattern $C_v(t) = e^{-t/\tau}$, where τ serves as the time constant for viscous motion [62–64]. Our findings, illustrated in Fig. 2(b) reveal VACF patterns across multiple data sets. At short timescales, VACFs display decays that are roughly exponential and analogous to those of Brownian particles across all data sets. However, diverging from the behavior of Brownian particles, VACF descends into negative territory before ultimately approaching zero.

To systematically quantify these behavioral timescales, we fit our empirical VACF data with the function $f(t) = Ae^{-t/\tau} - Be^{-t/\tau'}$, where the first and second terms represent the impacts of Brownian particles in a viscous fluid and interparticle interactions, respectively. Table I reveals that HC classrooms exhibit the lowest τ values, ranging between 0.5

TABLE I. Fitting parameters for empirical VACF with the function $f(t) = Ae^{-t/\tau} - Be^{-t/\tau'}$. A and B, respectively, denote the impacts of Brownian particles in a viscous fluid and the interparticle interactions. Similarly, τ and τ' are the time constants corresponding to viscous motion and interparticle interactions, respectively. S.E. refers to the corresponding standard error shown in parentheses.

Parameters (*Std. Error*)	*A (S.E.)*	*B (S.E.)*	τ [*s*](*S.E.*)	τ' [*s*](*S.E.*)
LC1	1.06 *(0.01)*	0.07 *(0.02)*	1.10 *(0.01)*	12.60 *(0.01)*
LC2	1.05 *(0.02)*	0.07 *(0.02)*	1.50 *(0.01)*	17.90 *(0.01)*
HC	1.05 *(0.01)*	0.05 *(0.06)*	0.60 *(0.01)*	8.30 *(0.03)*
PG	1.50 *(0.06)*	0.50 *(0.01)*	3.10 *(0.06)*	8.40 *(0.01)*

to 0.7s, when compared to LC1 and LC2, where τ varies between 0.8 to 1.6s. In contrast, individuals in PG settings manifest markedly slower and more extended VACFs with typical time constants of $2.5 - 2.6s$—nearly double the time constants observed in classroom settings (as seen in Fig. 2(b) and SM [55], Sec. B.2 for related statistical tests). This discrepancy occurs primarily in the PG data sets due to rapid or high-velocity movements that make it relatively challenging for individuals to alter their velocities on shorter timescales. This observation aligns with our hypothesis that playground environments are characterized by ballistic motions at a short timescale, with individuals generally maintaining their directions of movement.

Moreover, the occurrence of negative VACF values suggests that individuals tend to move in reverse at longer timescales, τ'. This behavior implies constraints imposed by social interactions among peers. Consistently, Table I reports τ' values on the order of magnitude of 10 s across all data sets, corroborating the MSD measurements. Furthermore, the VACF profiles for PGs show deeper negative values compared to those in classrooms, indicating a higher degree of anticorrelation [see Fig. 2(b)].

B. Structure measures

1. Radial distribution function

We measure the RDF, $g(r)$, the probability of finding a pair of individuals at distance r, relative to a random model of their position. $g(r) = 1$ indicates no pair correlations, where $g(r) > 1$ and $g(r) < 1$ correspond to attractive and repulsive pair interactions, respectively. Figure 2(c) illustrates the RDF for all data sets, revealing consistent patterns over settings. First, $g(r)$ is consistently peaked around $r_0 \approx 0.8$ m, suggesting a typical social contact distance regardless of settings. Second, social interaction is persistent over a broad range of distances, extending up to $2 - 3$ m, aligning with the observations from MSD.

In contrast, the values at which $g(r)$ peaks vary among different data sets, indicating variation in social interaction strength. The LCs have variable levels of social interaction strength but show greater interaction strengths than the HCs. Moreover, at greater distances, the classrooms and playgrounds manifest distinct behaviors: In PG, RDFs converge to unity at long distances, suggesting that individuals move freely and stay far from each other, as in a random walk model, a typical pattern for gas. On the other hand, the LCs $g(r)$ asymptotically descends below unity, which is evident in weaker form for HC. Radial distribution values below one suggest clustering tendencies because individuals are unlikely to be at a great distance from one another [4,5]. This implies that classroom data sets potentially entail small-sized social groups exhibiting strong correlations at short distances but anticorrelations at greater distances—a phenomenon often observed in the liquid-vapor coexistence phase [3,65,66].

2. Local density distribution

The observed anticorrelation in RDF at relatively large social distances, particularly in LC data sets, implies the formation of clusters at smaller length scales. No such clustering was observed for PG. To explore this distinction further, we measured the local population density that quantifies spatial variability (see SM [55], Sec. B.3). Figure 3 plots the LDD [67], $p(\rho)$, normalized by its mean, for all data sets. The LDD reveals a bimodality [53] in LC, where the peaks of high density in these regions imply an aggregation that may reflect attraction amongst individuals and the low-density peaks represent a more vaporlike activity. We find that $p(\rho)$ in LC1 and LC2 is well approximated by a bigamma distribution. Especially, the low-density peaks around $\rho_v = 0.1\bar{\rho} \sim 0.4\bar{\rho}$,

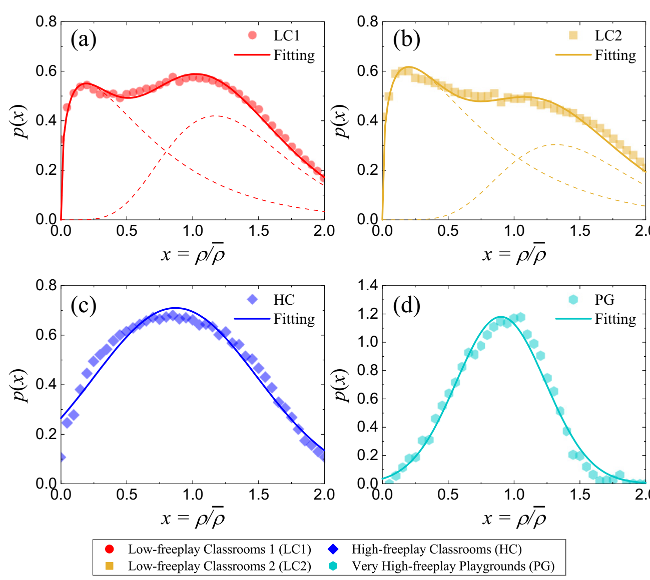

FIG. 3. Local density distribution. (a)–(d) represent local density distribution for data sets LC1, LC2, HC, and PG, respectively. Scatter plots in (a)–(d) represent the empirical measures. The colored curves in (a) and (b) represent the fitting curves of bigamma distribution, and the colored dashed curves represent two gamma distributions. The colored curves in (c) and (d) represent the fitting of a normal distribution.

high-density peaks around $\rho_l = 1.2\bar{\rho} \sim 1.40\bar{\rho}$ for LC1, and $\rho_v = 0.3\bar{\rho} \sim 0.5\bar{\rho}$ and $\rho_l = 1.3\bar{\rho} \sim 1.5\bar{\rho}$ for LC2.

By contrast, in the HC and PG groups, we observe robust unimodal distributions, with peaks centrally located around its mean $\bar{\rho}$. These unimodal patterns suggest a relatively uniform distribution of individuals throughout the space. Based on our observations, we note that the distribution pattern in all four settings may be influenced by the average speed of individuals within each system, and shows a gradual fading of bimodality as average speeds increase.

For molecular systems, when the system is in the gas phase, molecules move relatively freely and uniformly across space. However, in the liquid-vapor coexistence phase, the system comprises liquid droplets and vapors, the former having a notably higher density. Thus, a bimodal LLD emerges in this case, where the high-density peak corresponds to the liquid phase and the low-density peak corresponds to the gas phase [53].

Our empirical measurements suggest an analogy between molecular systems and the social systems in Figs. 3(a) and 3(b), suggesting the possible existence of multiple phases in human movements. Specifically, data sets exhibiting high moving speeds, such as HC and PG, indicate children moving rapidly, behaving like gas, and the absence of small social groups. By contrast, in LC1 and LC2, the bimodality of $p(\rho)$ may represent a liquid-vapor coexistence social phase, where the liquid phase signifies small social groups and the low-density peak depicts the background movement of individuals. The consistent presence of a social liquid phase might correspond to situations where individuals join and leave a social group relatively freely yet the group maintains dynamic stability.

IV. THEORETICAL MODEL AND NUMERICAL SIMULATIONS

Classical social force models propose that individuals' orientations significantly influence their social movement, conceptualizing individuals as moving magnets [68]. For example, the Vicsek model (VM) posits that the forces between two individuals i and j are governed by their relative orientations, provided their social distance r is less than a typical contact radius [49]. Specifically, it employs an orientational interaction similar to the one used in the classical XY model [63],

$$U(\mathbf{r}, \theta) = \sum_{i<j} J(r_{ij}) \cos(\theta_i - \theta_j), \qquad (1)$$

where $r_{ij} \equiv |\mathbf{r}_i - \mathbf{r}_j|$, and θ_i and θ_j represent their respective orientations. The coupling function $J(r)$ is the Heaviside step function, introducing a distinct spatial truncation at a boundary of a social contact radius. However, the RDF in the current data sets [Fig. 2(c)] suggests that real data exhibits more complexity than this idealized model. Rather than a distinct spatial truncation, the data implies variations in social behavior across different distances.

To quantify orientational interaction among participant pairs, we compute the angular correlation function [69] $C_\theta(r) = \langle \cos(\theta_i(0) - \theta_j(r)) \rangle$ that measures the alignment of pair angles as a function of separation distance r, averaged over all pairs. For instance, $C_\theta(r) = 1$ indicates a parallel alignment (side by side), i.e., $\theta_i = \theta_j$; whereas $C_\theta(r) = -1$ represents an opposite (face-to-face) alignment as $\theta_i = -\theta_j$. Figure 4(a) plots $C_\theta(r)$ for data sets LC1 and LC2, showing that $C_\theta(r)$ is positive when r is small and becomes negative at $r \approx 2 \sim 4$ m. When r becomes large, $C_\theta(r)$ approaches zero, indicating diminishing correlation or magnetic influence. This observation suggests that at short distances, individuals are more likely to be oriented parallel to each other, like ferromagnets, due to the contribution of side-by-side interactions. At longer distances, they tend to be oppositely oriented like antiferromagnets due to the domination of face-to-face interaction. The diminishing angular correlation at longer distances is a common feature of short-ranged interactions and is well-documented in existing studies. For instance, the celebrated Vicsek model assumes that the social force between particles is only applied to neighbors within a certain proximity (r_0), aligning them in the same direction [49]. However, the antiferromagnetic behavior at intermediate distance when the $C_\theta(r)$ becomes negative was not predicted by the VM or observed widely.

Inspired by these empirical observations, instead of the step function, we use the Morse potential [70] for the coupling function $J(r)$, which captures the empirical observation of ferromagnetic interaction at shorter distances and an antiferromagnetic interaction at longer distances [Fig. 4(a)]. In addition, we also used a soft sphere potential for each individual to take their physical size into consideration (see SM [55], Sec. C). Equation (1) applies to both passive and active particles [67]. Here we use a passive model for simplicity, which allows us to apply Monte Carlo simulations. We tested our model at different speeds and density values. We found that the proposed model reproduces radial distribution and angular correlation functions in qualitative agreement with empirical measurements (see SM [55], Sec. D.1). Moreover, for densities comparable to the observed empirical densities, we found monopeaked local density distributions for high-speed values corresponding to a gas phase [Fig. 4(b)], whereas bipeaked distributions for lower speed corresponding to a liquid-vapor coexistence phase [Fig. 4(c)]. The insets of Figs. 4(b) and 4(c) demonstrate snapshots of movement patterns for these two phases [71,72].

While existing models suggest a similar liquid-vapor phase transition [27], these transitions are often coupled with a change of orientational order. We measured the magnetization order parameter $\frac{\langle M \rangle}{N} = \frac{1}{N} |\langle s \rangle| \equiv \frac{1}{N} |\langle (\sum_{i=1}^{N} \cos\theta_i, \sum_{i=1}^{N} \sin\theta_i) \rangle|$ for LC data sets, which quantifies the collective polarization of the individual's orientation. We find $m_0 \approx 0.001$ and 0.002 for LC1 and LC2, respectively, suggesting that the orientations of children are disordered over all directions. Therefore, unlike the existing models [24,27], the observed liquid-vapor phase transition is not accompanied by orientational order changes, partly due to the mixture of ferro- and antiferromagnetic orders at different distances. Likewise, there are no orientational order changes during the liquid-vapor phase transition in our model, in line with empirical observations.

Figure 5 presents the social phase diagram as estimated by our model, based on numerical simulations. The diagram is highlighted by a gradient gray area, which roughly estimates

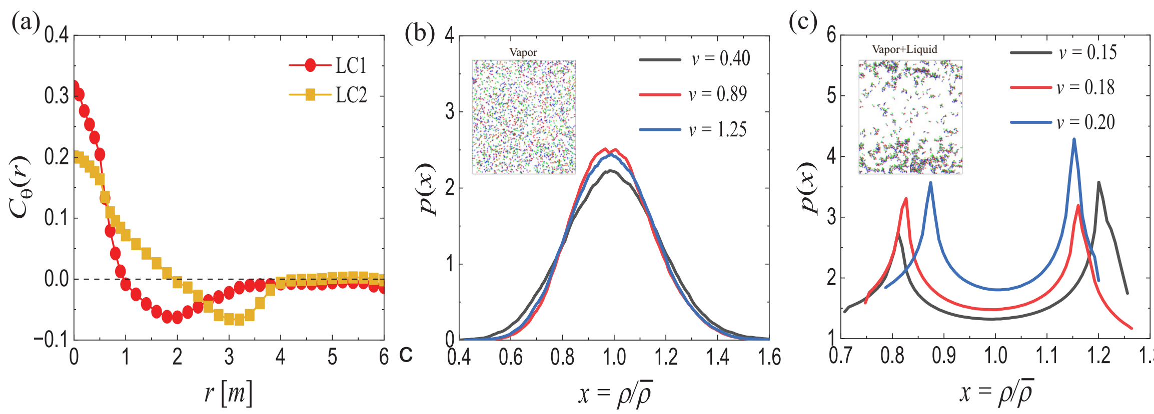

FIG. 4. Numerical simulation. (a) Angular correlation function measures for LC1 and LC2. (b), (c) Local density distributions of the proposed model with relatively high and low average speeds, at a density of 0.25 m^{-2}, respectively. Insets in (b) and (c) show snapshots of the corresponding systems.

the liquid-vapor coexistence phase. The intention here is not to pinpoint an exact boundary but to visually depict the different phases. Notably, LC1 is positioned within the liquid-vapor coexistence regime, indicative of a bipeaked LDD. Conversely, LC2 is located near the coexistence region's boundary. Although LC2's speeds are similar to those in the simulations, its lower densities result in less pronounced bimodalities in the LDD measure. Regarding HC and PG, their average speeds exceed the phase coexistence threshold, thereby not exhibiting any bipeaked distribution. However, it is important to note that a few empirical data points for HC do not strictly conform to the simulated boundary, indicating that while the simulation provides a useful guideline, it may not capture all nuances of the empirical data. We believe that there are multiple modes of interactions involving orientations in our system that go beyond the typical *XY*-like attractive interactions. The interplay of these complex orientational interactions can be better captured quantitatively by incorporating additional terms in the potential function, which we will leave for future investigations.

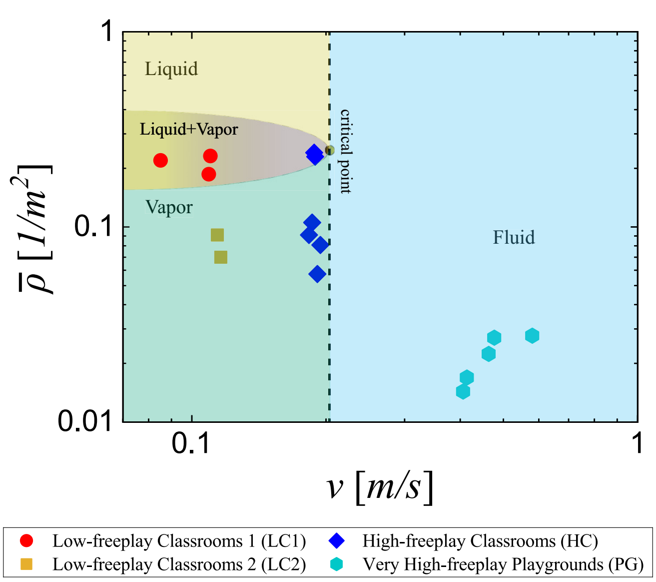

FIG. 5. Phase diagram. The dots represent empirical data, and the phase boundary, indicated by the gray curve, is estimated through numerical simulation of the simple model.

V. DISCUSSION

In physical systems, microscopic properties undergo continuous changes and, as a result, macroscopic systems exhibit emergent changes in their phases. Theoretically, similar phenomena might arise in social systems characterized by human interactions and movements, a hypothesis posited two decades ago [53]. Earlier studies of traffic and pedestrian flows primarily focused on relatively high-speed mobility data where pairwise interactions were weak. While different hydrodynamic phases in traffic flows based on moving speed have been observed [31–33,73], the social phase of collective condensation arising from interactions among individuals has not been previously observed. By contrast, the present paper delves into a largely unexplored parameter space. Specifically, we analyze empirical data sets detailing children's mobility patterns in preschools, covering both classroom and playground movements. These data sets encompass lower speed regimes, roughly an order of magnitude below those of previous studies.

Quantitative parameters including the mean square displacement, the velocity autocorrelation function, the radial distribution function, and the local density distribution suggest that children's movements may be divided into two distinct social phases, i.e., a liquid-vapor coexistencelike phase and a gaslike phase, which reflects differences in quantified school activities. The key variable appears to be the proportion of the observation period dedicated to free play in which children were able to move where they pleased. This appeared to reduce the children's mobility, allowing the formation of small, dynamically stable social groups similar to liquid droplets. Free-moving individuals may join and leave these social groups with relatively high mobility, similar to vapor in the coexistence phase. By contrast, in the high free-play classrooms and very high free-play playgrounds, the state of the system to be more vapor- or gaslike.

The current research is an example of social physics, an attempt to rigorously model human behavior based on recent sensing technologies and innovative theoretical perspectives [9,12]. Our paper provides experimental evidence from real-time continuous observation of the existence of multiple social phases in human movements [53]. Future research is required to experimentally manipulate control parameters such as average speed of social movement or to effectively implement a temperature-type measure in molecular systems that are hypothesized to control these phase transitions. As noted by Ref. [3], such an effective temperature measure described here could also enrich our understanding of phase coexistence in insects and other social animals. The results shed light on the physics of social interactions in human movement, with potential implementations for fields including behavioral science [74], biological science [3–7], and epidemiology [13].

ACKNOWLEDGMENTS

This work was partially supported by the National Science Foundation under Grants No. 2150830 and No. IBSS-1620294, the Institute of Education Sciences under Grant No. R324A180203, the National Institutes of Health under Grant No. R01DC018542, the Marcus Autism Center, Children's Healthcare of Atlanta, and the Simons Foundation for Autism Research Initiative under Grant No. SFI-AR-HUMAN-00004115-01. We would also like to acknowledge the involvement of Emory University's Pediatric Biostatistics Core.

Y.Z. and D.S. contributed equally to this work.

The authors declare no conflicts of interest.

[1] J. K. Parrish and L. Edelstein-Keshet, Complexity, pattern, and evolutionary trade-offs in animal aggregation, Science **284**, 99 (1999).

[2] H.-P. Zhang, A. Be'er, E.-L. Florin, and H. L. Swinney, Collective motion and density fluctuations in bacterial colonies, Proc. Natl. Acad. Sci. USA **107**, 13626 (2010).

[3] M. Sinhuber and N. T. Ouellette, Phase coexistence in insect swarms, Phys. Rev. Lett. **119**, 178003 (2017).

[4] A. Attanasi, A. Cavagna, L. Del Castello, I. Giardina, S. Melillo, L. Parisi, O. Pohl, B. Rossaro, E. Shen, E. Silvestri *et al.*, Collective behaviour without collective order in wild swarms of midges, PLoS Comput. Biol. **10**, e1003697 (2014).

[5] A. Attanasi, A. Cavagna, L. Del Castello, I. Giardina, S. Melillo, L. Parisi, O. Pohl, B. Rossaro, E. Shen, E. Silvestri *et al.*, Finite-size scaling as a way to probe near-criticality in natural swarms, Phys. Rev. Lett. **113**, 238102 (2014).

[6] Y. Katz, K. Tunstrøm, C. C. Ioannou, C. Huepe, and I. D. Couzin, Inferring the structure and dynamics of interactions in schooling fish, Proc. Natl. Acad. Sci. USA **108**, 18720 (2011).

[7] J. E. Herbert-Read, A. Perna, R. P. Mann, T. M. Schaerf, D. J. Sumpter, and A. J. Ward, Inferring the rules of interaction of shoaling fish, Proc. Natl. Acad. Sci. USA **108**, 18726 (2011).

[8] W. Bialek, A. Cavagna, I. Giardina, T. Mora, E. Silvestri, M. Viale, and A. M. Walczak, Statistical mechanics for natural flocks of birds, Proc. Natl. Acad. Sci. USA **109**, 4786 (2012).

[9] M. Perc, The social physics collective, Sci. Rep. **9**, 16549 (2019).

[10] T. Vicsek and A. Zafeiris, Collective motion, Phys. Rep. **517**, 71 (2012).

[11] A. Corbetta and F. Toschi, Physics of human crowds, Annu. Rev. Condens. Matter Phys. **14**, 311 (2023).

[12] M. Jusup, P. Holme, K. Kanazawa, M. Takayasu, I. Romić, Z. Wang, S. Geček, T. Lipić, B. Podobnik, L. Wang *et al.*, Social physics, Phys. Rep. **948**, 1 (2022).

[13] Y. Zhang, Y. Tao, M.-L. Shyu, L. K. Perry, P. R. Warde, D. S. Messinger, and C. Song, Simulating COVID-19 transmission from observed movement, Sci. Rep. **12**, 3044 (2022).

[14] I. Zuriguel, A. Garcimartín, and R. C. Hidalgo, *Traffic and Granular Flow 2019* (Springer, Cham, Switzerland, 2020), pp. 249–255.

[15] I. Ali and M. N. Dailey, Multiple human tracking in high-density crowds, Image Vision Comput. **30**, 966 (2012).

[16] R. Sundararaman, C. De Almeida Braga, E. Marchand, and J. Pettre, Tracking pedestrian heads in dense crowd, in *Proceedings of the IEEE/CVF Conference on Computer Vision and Pattern Recognition (CVPR)* (IEEE, Piscataway, NJ, 2021), pp. 3865–3875.

[17] V. Sekara, A. Stopczynski, and S. Lehmann, Fundamental structures of dynamic social networks, Proc. Natl. Acad. Sci. USA **113**, 9977 (2016).

[18] A. Corbetta, J. A. Meeusen, C.-M. Lee, R. Benzi, and F. Toschi, Physics-based modeling and data representation of pairwise interactions among pedestrians, Phys. Rev. E **98**, 062310 (2018).

[19] S. Seer, N. Brändle, and C. Ratti, Kinects and human kinetics: A new approach for studying pedestrian behavior, Transp. Res. Part C Emerg. **48**, 212 (2014).

[20] A. Corbetta, J. Meeusen, C.-m. Lee, and F. Toschi, Continuous measurements of real-life bidirectional pedestrian flows on a wide walkway, arXiv:1607.02897.

[21] W. Song, J. Ma, and L. Fu, Proceedings of pedestrian and evacuation dynamics 2016, Collect. Dyn. **1**, 618 (2016).

[22] D. Brockmann, L. Hufnagel, and T. Geisel, The scaling laws of human travel, Nature (London) **439**, 462 (2006).

[23] M. C. Gonzalez, C. A. Hidalgo, and A.-L. Barabasi, Understanding individual human mobility patterns, Nature (London) **453**, 779 (2008).

[24] C. Song, T. Koren, P. Wang, and A.-L. Barabási, Modelling the scaling properties of human mobility, Nat. Phys. **6**, 818 (2010).

[25] F. Simini, M. C. González, A. Maritan, and A.-L. Barabási, A universal model for mobility and migration patterns, Nature (London) **484**, 96 (2012).

[26] J. A. Firth, J. Hellewell, P. Klepac, S. Kissler, A. J. Kucharski, and L. G. Spurgin, Using a real-world network to model localized COVID-19 control strategies, Nat. Med. **26**, 1616 (2020).

[27] M. Nagy, Z. Ákos, D. Biro, and T. Vicsek, Hierarchical group dynamics in pigeon flocks, Nature (London) **464**, 890 (2010).

[28] B. Piccoli and A. Tosin, Pedestrian flows in bounded domains with obstacles, Continuum Mech. Thermodyn. **21**, 85 (2009).

[29] A. Seyfried, B. Steffen, and T. Lippert, Basics of modelling the pedestrian flow, Physica A **368**, 232 (2006).
[30] S. Hoogendoorn and W. Daamen, Self-organization in pedestrian flow, in *Traffic and Granular Flow '03* (Springer, Berlin, Heidelberg, Germany, 2005), pp. 373–382.
[31] L. Henderson, The statistics of crowd fluids, Nature (London) **229**, 381 (1971).
[32] L. Henderson and D. Lyons, Sexual differences in human crowd motion, Nature (London) **240**, 353 (1972).
[33] L. F. Henderson, On the fluid mechanics of human crowd motion, Transp. Res. **8**, 509 (1974).
[34] F. Zanlungo, T. Ikeda, and T. Kanda, Potential for the dynamics of pedestrians in a socially interacting group, Phys. Rev. E **89**, 012811 (2014).
[35] D. Brščić, F. Zanlungo, and T. Kanda, Density and velocity patterns during one year of pedestrian tracking, Transp. Res. Proc. **2**, 77 (2014).
[36] H. Murakami, C. Feliciani, and K. Nishinari, Lévy walk process in self-organization of pedestrian crowds, J. R. Soc. Interface. **16**, 20180939 (2019).
[37] N. Bain and D. Bartolo, Dynamic response and hydrodynamics of polarized crowds, Science **363**, 46 (2019).
[38] C. Feliciani and K. Nishinari, Empirical analysis of the lane formation process in bidirectional pedestrian flow, Phys. Rev. E **94**, 032304 (2016).
[39] M. Moussaïd, E. G. Guillot, M. Moreau, J. Fehrenbach, O. Chabiron, S. Lemercier, J. Pettré, C. Appert-Rolland, P. Degond, and G. Theraulaz, Traffic instabilities in self-organized pedestrian crowds, PLoS Comput. Biol. **8**, e1002442 (2012).
[40] A. Tordeux, M. Chraibi, A. Seyfried, and A. Schadschneider, Prediction of pedestrian dynamics in complex architectures with artificial neural networks, J. Intell. Transp. Syst. **24**, 556 (2020).
[41] H. Yamamoto, D. Yanagisawa, C. Feliciani, and K. Nishinari, Body-rotation behavior of pedestrians for collision avoidance in passing and cross flow, Transp. Res. Part B: Methodol. **122**, 486 (2019).
[42] J. Willems, A. Corbetta, V. Menkovski, and F. Toschi, Pedestrian orientation dynamics from high-fidelity measurements, Sci. Rep. **10**, 11653 (2020).
[43] Y.-f. Wei, D.-k. Lan, and L.-y. Dong, Fundamental diagrams for pedestrian flows in a channel via an extended social force model, J. Hydrodyn. **30**, 950 (2018).
[44] D. R. Parisi, A. G. Sartorio, J. R. Colonnello, A. Garcimartín, L. A. Pugnaloni, and I. Zuriguel, Pedestrian dynamics at the running of the bulls evidence an inaccessible region in the fundamental diagram, Proc. Natl. Acad. Sci. USA **118**, e2107827118 (2021).
[45] B. Hankin and R. A. Wright, Passenger flow in subways, J. Oper. Res. Soc. **9**, 81 (1958).
[46] Y. Shang, Consensus in averager-copier-voter networks of moving dynamical agents, Chaos **27**, 023116 (2017).
[47] D. S. Messinger, E. B. Prince, M. Zheng, K. Martin, S. G. Mitsven, S. Huang, T. Stölzel, N. Johnson, U. Rudolph, L. K. Perry *et al.*, Continuous measurement of dynamic classroom social interactions, Int. J. Behav. Dev. **43**, 263 (2019).
[48] R. M. Fasano, L. K. Perry, Y. Zhang, L. Vitale, J. Wang, C. Song, and D. S. Messinger, A granular perspective on inclusion: Objectively measured interactions of preschoolers with and without autism, Autism Res. **14**, 1658 (2021).
[49] T. Vicsek, A. Czirók, E. Ben-Jacob, I. Cohen, and O. Shochet, Novel type of phase transition in a system of self-driven particles, Phys. Rev. Lett. **75**, 1226 (1995).
[50] D. Helbing and P. Molnar, Social force model for pedestrian dynamics, Phys. Rev. E **51**, 4282 (1995).
[51] D. Helbing, I. Farkas, and T. Vicsek, Simulating dynamical features of escape panic, Nature (London) **407**, 487 (2000).
[52] D. Helbing, Traffic and related self-driven many-particle systems, Rev. Mod. Phys. **73**, 1067 (2001).
[53] G. Grégoire and H. Chaté, Onset of collective and cohesive motion, Phys. Rev. Lett. **92**, 025702 (2004).
[54] Y. Shang, A system model of three-body interactions in complex networks: Consensus and conservation, Proc. R. Soc. A **478**, 20210564 (2022).
[55] See Supplemental Material at http://link.aps.org/supplemental/10.1103/PhysRevE.110.044303 for details on the experimental setup, data set descriptions, dynamic measures, statistical tests, and numerical simulations supporting this paper.
[56] A. Matakos, E. Terzi, and P. Tsaparas, Measuring and moderating opinion polarization in social networks, Data Mining Knowl. Discovery **31**, 1480 (2017).
[57] D. W. Irvin, S. A. Crutchfield, C. R. Greenwood, W. D. Kearns, and J. Buzhardt, An automated approach to measuring child movement and location in the early childhood classroom, Behav. Res. Methods **50**, 890 (2018).
[58] L. Barbieri, M. Brambilla, A. Trabattoni, S. Mervic, and M. Nicoli, UWB localization in a smart factory: Augmentation methods and experimental assessment, IEEE Trans. Instrum. Meas. **70**, 1 (2021).
[59] R. E. Kalman, A new approach to linear filtering and prediction problems, J. Basic Eng. **82**, 35 (1960).
[60] G. Bishop and G. Welch, An introduction to the Kalman filter, Proc. SIGGRAPH. Course **8**, 41 (2001).
[61] R. Kubo, M. Toda, and N. Hashitsume, *Statistical Physics II: Nonequilibrium Statistical mechanics* (Springer Science & Business Media, Berlin, Heidelberg, Germany, 2012), Vol. 31.
[62] R. Kubo, The fluctuation-dissipation theorem, Rep. Prog. Phys. **29**, 255 (1966).
[63] J. A. Leegwater, Velocity autocorrelation function of Lennard-Jones fluids, J. Chem. Phys. **94**, 7402 (1991).
[64] T. Li and M. G. Raizen, Brownian motion at short time scales, Ann. Phys. **525**, 281 (2013).
[65] J. P. Doye and D. J. Wales, The effect of the range of the potential on the structure and stability of simple liquids: From clusters to bulk, from sodium to C_{60}, J. Phys. B: At. Mol. Opt. Phys. **29**, 4859 (1996).
[66] K. Mochizuki and K. Koga, Solid-liquid critical behavior of water in nanopores, Proc. Natl. Acad. Sci. USA **112**, 8221 (2015).
[67] J.-P. Hansen and I. R. McDonald, *Theory of Simple Liquids: With Applications to Soft Matter*, 4th ed. (Academic Press, New York, 2013).
[68] R. Loft and T. A. DeGrand, Numerical simulation of dynamics in the *XY* model, Phys. Rev. B **35**, 8528 (1987).
[69] K. Nho and D. P. Landau, Spin-dynamics simulations of the triangular antiferromagnetic *XY* model, Phys. Rev. B **66**, 174403 (2002).
[70] I. G. Kaplan, *Intermolecular Interactions: Physical Picture, Computational Methods and Model Potentials* (John Wiley & Sons, Chichester, West Sussex, England, 2006).

[71] H. E. Stanley, *Phase Transitions and Critical Phenomena* (Clarendon Press, Oxford, 1971), Vol. 7.

[72] J. V. Jos, *40 Years of Berezinskii-Kosterlitz-Thouless Theory* (World Scientific, Singapore, 2013).

[73] J. Zhang, W. Mehner, S. Holl, M. Boltes, E. Andresen, A. Schadschneider, and A. Seyfried, Universal flow-density relation of single-file bicycle, pedestrian and car motion, Phys. Lett. A **378**, 3274 (2014).

[74] N. M. Saragosa-Harris, A. O. Cohen, T. R. Reneau, W. J. Villano, A. S. Heller, and C. A. Hartley, Real-world exploration increases across adolescence and relates to affect, risk taking, and social connectivity, Psychol. Sci. **33**, 1664 (2022).